Comput Geosci (2015) 19:327–340
DOI 10.1007/s10596-015-9472-0

ORIGINAL PAPER

High-order finite difference modeling of tsunami generation in a compressible ocean from offshore earthquakes

Gabriel C. Lotto · Eric M. Dunham

Received: 28 April 2014 / Accepted: 4 February 2015 / Published online: 12 March 2015

Abstract To study the full seismic, ocean acoustic, and tsunami wavefields generated by subduction zone earthquakes, we have developed a provably stable and accurate finite difference method that couples an elastic solid to a compressible fluid subject to gravitational restoring forces. We introduce a linearized dynamic traction-free boundary condition for the moving sea surface that is valid for small amplitude perturbations about an ocean initially in hydrostatic balance. We derive an energy balance for the continuous problem and then use high-order summation-by-parts finite difference operators and weak enforcement of boundary conditions to derive an equivalent discrete energy balance. The discrete energy balance is used to prove stability of the numerical scheme, and stability and accuracy are verified through convergence tests. The method is applied to study tsunami generation by time-dependent rupture on a thrust fault in an elastic solid beneath a compressible ocean. We compare the sea surface evolution in our model to that predicted by the standard tsunami modeling procedure, which assumes seafloor uplift occurs instantaneously and neglects compressibility of the ocean. We find that the leading shoreward-traveling tsunami wave in our model has a noticeably smaller amplitude than that predicted by the standard approach.

Keywords Tsunami · Surface gravity waves · Ocean acoustic waves · Seismic waves · Subduction zone earthquakes · Summation by parts

1 Introduction

In recent years, the world has twice witnessed the devastation that a large tsunami can cause. Taken together, the 26 December 2004 Indian Ocean tsunami and the 11 March 2011 Tohoku, Japan, tsunami claimed hundreds of thousands of lives and caused immense damage [16, 18]. Tsunamis of such enormity can occur as a result of megathrust earthquakes when shallow coseismic slip causes seafloor uplift, displacing the ocean and exciting surface gravity waves. We would like to better understand the general problem of tsunami generation in a compressible ocean with realistic geometry due to a time-dependent rupture process on a fault.

As further motivation, the shallow slip that generates tsunami waves also excites a wide range of seismic and ocean acoustic waves [6, 14]. Of special interest are leaking P-wave modes that are comprised of multiply-reflected sound waves filling the entire depth of the ocean and seismic waves penetrating ∼10 km into the solid. The amplitudes of these waves correlate well with seafloor uplift at the trench [7] and, thus, with tsunami heights. These guided waves travel at several kilometers per second and reach the coast many minutes sooner than tsunami waves [15, 17]; these waves could potentially be used to improve local early warning systems for tsunami-prone regions.

This work was supported by the National Science Foundation (EAR-1255439) and the Alfred P. Sloan Foundation (BR2012-097).

G. C. Lotto (✉)
Department of Geophysics, Stanford University, 397 Panama Mall, Stanford, CA 94305, USA
e-mail: glotto@stanford.edu

E. M. Dunham
Department of Geophysics and Institute for Computational and Mathematical Engineering, Stanford University, 397 Panama Mall, Stanford, CA 94305, USA

Addressing these problems requires simulation methods that rigorously couple the elastodynamic response of the solid earth with that of a compressible ocean in the presence of gravity. Maeda and Furumura [13] were the first to develop such a method using a staggered grid finite difference scheme. Their approach modifies the momentum balance equations throughout the medium through the addition of terms involving spatial derivatives of the sea surface height. Calculating those derivatives at the surface and communicating their values to all other grid points below increases the computational cost and limits parallel scalability. We present an alternative approach that introduces no additional terms to the governing equations and requires only a minor modification of the free surface boundary condition at the sea surface. Our method has been implemented in our 2-D finite difference code that handles complex geometries, heterogeneous material properties, and earthquake rupture dynamics [6, 7, 9].

This paper extends the work done by Kozdon and Dunham [9]; our novel contribution is the introduction of a new free surface boundary condition on the moving sea surface valid for small amplitude perturbations about an ocean initially in hydrostatic balance. We can now model tsunami waves in the linearized theory in the same code as elastic and ocean acoustic waves. The code uses high order summation-by-parts (SBP) finite difference operators for spatial discretization and a 4th-order low-storage Runge-Kutta method in time. Modeling tsunamis accurately requires taking hundreds of thousands of time steps , so we must be able to guarantee the absence of spurious sources or sinks of energy. SBP finite difference methods are very useful because they allow us to derive a numerical energy balance that mimics the continuous energy balance and allows us to explicitly prove the stability of our numerical method.

In this paper, we first present the continuous governing equations for wave propagation in a 2-D ocean layer with a free surface upper boundary condition in the presence of a gravitational field. We derive an energy balance for this system that establishes conservation of energy. Next, we spatially discretize the same governing equations using high-order SBP finite difference operators and weakly enforce boundary conditions using the simultaneous approximation term (SAT) method. This allows us to establish a discrete energy balance that closely parallels the continuous version, providing a means to prove stability of the overall method. We present convergence tests verifying the accuracy of the method for analytical modal solutions to the governing equations in a rigid-bottomed compressible ocean. We then apply the method to study generation of seismic, ocean acoustic, and seismic waves by rupture on a thrust fault in an elastic solid beneath the ocean. Comparisons are made to both an analytical solution for seafloor displacement and to the evolution of the surface gravity waves using an incompressible ocean theory.

2 Continuous problem

Consider a compressible ocean of initially uniform depth H (Fig. 1), subject to 2-D perturbations. Let x and y be the horizontal and vertical coordinates in an Eulerian description with $y = 0$ being the unperturbed ocean surface. The ocean is initially in hydrostatic balance, for which pressure $p_0 = p_0(y)$ and density $\rho_0 = \rho_0(y)$ satisfy

$$\frac{\mathrm{d}p_0}{\mathrm{d}y} = -\rho_0 g, \tag{1}$$

where g is the gravitational acceleration. Density and pressure are also linked by an equation of state. Introducing K_0 as the bulk modulus in this hydrostatic state, we have

$$\frac{1}{\rho_0}\frac{\mathrm{d}\rho_0}{\mathrm{d}y} = \frac{1}{K_0}\frac{\mathrm{d}p_0}{\mathrm{d}y}. \tag{2}$$

We next consider perturbations about this hydrostatic state. The perturbed ocean surface is $y = \eta(x,t)$ and the perturbed seafloor lies at $y = -H + b(x,t)$, and we denote the horizontal and vertical particle velocities as $u(x,y,t)$ and $v(x,y,t)$, respectively. We also express the pressure, $p(x,y,t)$, as the sum of the initial hydrostatic pressure, $p_0(y)$, and a perturbation, $p'(x,y,t)$; that is, $p = p_0 + p'$, with a similar notation for density.

Differentiating the equation of state following a fluid parcel and linearizing yields

$$\frac{1}{\rho_0}\left(\frac{\partial \rho'}{\partial t} + v\frac{\mathrm{d}\rho_0}{\mathrm{d}y}\right) = \frac{1}{K}\left(\frac{\partial p'}{\partial t} + v\frac{\mathrm{d}p_0}{\mathrm{d}y}\right). \tag{3}$$

Here, K is the bulk modulus of the fluid at the short time scales describing wave motions, over which transport of heat and salinity is negligible. For this reason, K is potentially different than K_0, but in this work, we assume $K_0 = K$. Then, inserting Eq. 2 in Eq. 3 and integrating in

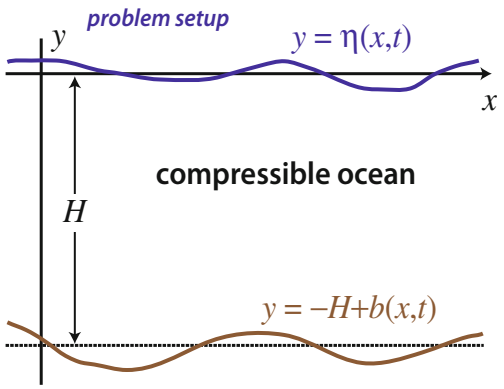

Fig. 1 Geometry for the continuous problem

time at fixed y, we obtain a simple proportionality between density and pressure perturbations:

$$\rho'/\rho_0 = p'/K. \tag{4}$$

The momentum balance equations for an inviscid fluid linearized about a state of rest satisfying hydrostatic balance (Eq. 1) are

$$\rho_0 \frac{\partial u}{\partial t} + \frac{\partial p'}{\partial x} = 0, \quad \rho_0 \frac{\partial v}{\partial t} + \frac{\partial p'}{\partial y} = -\rho' g. \tag{5}$$

Using Eq. 4 in Eq. 5 yields

$$\rho_0 \frac{\partial u}{\partial t} + \frac{\partial p'}{\partial x} = 0, \quad \rho_0 \frac{\partial v}{\partial t} + \frac{\partial p'}{\partial y} = -\frac{\rho_0 g}{K} p'. \tag{6}$$

The linearized mass balance is

$$\frac{1}{\rho_0}\left(\frac{\partial \rho'}{\partial t} + v\frac{\mathrm{d}\rho_0}{\mathrm{d}y}\right) + \frac{\partial u}{\partial x} + \frac{\partial v}{\partial y} = 0. \tag{7}$$

Using Eqs. 1–3 in Eq. 7 yields

$$\frac{1}{K}\frac{\partial p'}{\partial t} + \frac{\partial u}{\partial x} + \frac{\partial v}{\partial y} = \frac{\rho_0 g}{K} v. \tag{8}$$

Next, we state boundary conditions. The dynamic boundary condition sets pressure to atmospheric pressure p_a on the moving sea surface:

$$p(x, \eta(x,t), t) = p_a. \tag{9}$$

Rigorously enforcing (9) would require the introduction of a time-dependent curvilinear mesh. Doing so would not only be very difficult, but is unnecessary for the accurate modeling of tsunamis and surface gravity waves where wave amplitude $|\eta|$ is much smaller than the horizontal wavelength or water depth, whichever is smaller; the small amplitude approximation is well justified away from the immediate vicinity of the coast. We exploit the small wave amplitudes to linearize the boundary condition (9), as is typical for these problems [12]. Our immediate objective is to enforce this condition on the unperturbed sea surface, $y = 0$, since that allows us to use a fixed mesh. Assuming $\eta(x,t)$ is small, we take the first two terms of a Taylor expansion of p about $y = 0$:

$$p(x, \eta(x,t), t) \approx p(x, 0, t) + \left.\frac{\partial p}{\partial y}\right|_{y=0} \eta(x,t). \tag{10}$$

In this linearized analysis, it suffices to evaluate the vertical pressure gradient in the hydrostatic state (1). Thus, to first-order accuracy,

$$p(x, 0, t) = p_a + \rho_0(0) g \eta(x,t). \tag{11}$$

Writing $p = p_0 + p'$ and recognizing that $p_0(0) = p_a$ in the hydrostatic state, we obtain

$$p'(x, 0, t) = \rho_0(0) g \eta(x,t). \tag{12}$$

The link between sea surface height η and particle velocities u and v comes from the kinematic condition:

$$v(x, \eta(x,t), t) = \frac{\partial \eta}{\partial t} + u(x, \eta(x,t), t)\frac{\partial \eta}{\partial x}. \tag{13}$$

Equation 13 can be linearized to

$$\frac{\partial \eta}{\partial t} = v(x, 0, t), \tag{14}$$

again using the small amplitude approximation.

In this and the following section, the seafloor displacement $b(x,t)$ is imposed to excite waves in the ocean. The extension to the more general class of problems involving coupling between the ocean and underlying solid and to the case of complex geometries can be done following Kozdon et al. [9] and will not be repeated here. For imposed motion of an initially horizontal seafloor, the kinematic condition relating b, u, and v at the seafloor can also be linearized:

$$\frac{\partial b}{\partial t} = v(x, -H, t). \tag{15}$$

In this work, we neglect the slight depth dependence of density (and possibly also of bulk modulus and sound speed). We work with u, v, p', and η as our unknown fields, and in the remainder of this work, to simplify notation, we now use p to refer to pressure perturbations and ρ to refer to the (constant) density. The governing equations are summarized, in this new notation, as

$$\rho \frac{\partial u}{\partial t} + \frac{\partial p}{\partial x} = 0, \tag{16}$$

$$\rho \frac{\partial v}{\partial t} + \frac{\partial p}{\partial y} = -\frac{\rho g}{K} p, \tag{17}$$

$$\frac{1}{K}\frac{\partial p}{\partial t} + \frac{\partial u}{\partial x} + \frac{\partial v}{\partial y} = \frac{\rho g}{K} v, \tag{18}$$

and the boundary conditions as

$$p(x, 0, t) = \rho g \eta(x,t). \tag{19}$$

$$\frac{\partial \eta}{\partial t} = v(x, 0, t), \tag{20}$$

$$\frac{\partial b}{\partial t} = v(x, -H, t). \tag{21}$$

The sound speed is defined in terms of the bulk modulus K and density ρ as $c = \sqrt{K/\rho}$.

Note that governing Eqs. 16–18 are identical to those of classical acoustics when the terms on the right sides of Eqs. 17 and 18 are set to zero. Those terms are quite small compared to the other terms in those equations for parameter values appropriate to earth's oceans. Scaling arguments show that both terms provide small corrections at most of order $\rho g H/K = gH/c^2 \ll 1$, and we neglect those terms in the remainder of this work.

2.1 Continuous energy balance

Below, we derive the energy balance for the continuous problem. We write the momentum balance equations in vector form, take the dot product of each side with particle velocity $\mathbf{v}$, and integrate over the total area to get

$$\int_{-H}^{0}\int_{-\infty}^{\infty}\rho\mathbf{v}\cdot\frac{\partial\mathbf{v}}{\partial t}\,\mathrm{d}x\mathrm{d}y=-\int_{-H}^{0}\int_{-\infty}^{\infty}\mathbf{v}\cdot\nabla p\,\mathrm{d}x\mathrm{d}y. \quad (22)$$

It suffices to integrate over the unperturbed ocean; integrating between $y=-H+b$ and $y=\eta$ would introduce negligible, higher-order terms. Integrating the right side of Eq. 22 by parts in both x and y and substituting Eq. 18 yields

$$\int_{-H}^{0}\int_{-\infty}^{\infty}\rho\mathbf{v}\cdot\frac{\partial\mathbf{v}}{\partial t}\,\mathrm{d}x\mathrm{d}y=-\frac{1}{K}\int_{-H}^{0}\int_{-\infty}^{\infty}p\,\frac{\partial p}{\partial t}\,\mathrm{d}x\mathrm{d}y -\int_{-\infty}^{\infty}\left(vp\big|_{-H}^{0}\right)\mathrm{d}x-\int_{-H}^{0}\left(up\big|_{-\infty}^{\infty}\right)\mathrm{d}y. \quad (23)$$

We assume that waves have not yet reached $x=\pm\infty$ so that $u=0$ and $p=0$ at the horizontal boundaries, so we eliminate the last term of Eq. 23 and rewrite it as

$$\begin{aligned}\int_{-H}^{0}\int_{-\infty}^{\infty}\rho\mathbf{v}\cdot\frac{\partial\mathbf{v}}{\partial t}\,\mathrm{d}x\mathrm{d}y&=-\frac{1}{K}\int_{-H}^{0}\int_{-\infty}^{\infty}p\,\frac{\partial p}{\partial t}\,\mathrm{d}x\mathrm{d}y-\int_{-\infty}^{\infty}\left(vp\big|_{0}-vp\big|_{-H}\right)\mathrm{d}x\\&=-\frac{1}{K}\int_{-H}^{0}\int_{-\infty}^{\infty}p\,\frac{\partial p}{\partial t}\,\mathrm{d}x\mathrm{d}y-\rho g\int_{-\infty}^{\infty}\eta\,\frac{\partial\eta}{\partial t}\,\mathrm{d}x+\int_{-\infty}^{\infty}\frac{\partial b}{\partial t}\,p\Big|_{-H}\mathrm{d}x, \quad (24)\end{aligned}$$

where for the last step, we used Eqs. 20, 21, and 19.

We rewrite Eq. 24 so that terms in the form of $\mathbf{v}\cdot\partial\mathbf{v}/\partial t$ appear as $(1/2)\partial(\mathbf{v}^2)/\partial t$:

$$\frac{d}{dt}\left[\int_{-H}^{0}\int_{-\infty}^{\infty}\frac{1}{2}\rho\mathbf{v}^2\,\mathrm{d}x\mathrm{d}y+\int_{-H}^{0}\int_{-\infty}^{\infty}\frac{1}{2K}p^2\,\mathrm{d}x\mathrm{d}y+\int_{-\infty}^{\infty}\frac{1}{2}\rho g\eta^2\,\mathrm{d}x\right]=\int_{-\infty}^{\infty}\frac{\partial b}{\partial t}\,p\Big|_{-H}\mathrm{d}x. \quad (25)$$

We recognize the first integral of Eq. 25 as the kinetic energy of the system (KE) and the second integral as acoustic energy (AE). The third term represents the change in gravitational potential energy (GE), which is clear if we integrate the gravitational potential energy density, ρgy, over a column of ocean and take the time derivative:

$$\frac{\partial}{\partial t}\left(\rho g\int_{-H}^{\eta}y\mathrm{d}y\right)=\frac{\rho g}{2}\frac{\partial}{\partial t}\left(\eta^2-H^2\right)=\frac{\rho g}{2}\frac{\partial}{\partial t}\eta^2. \quad (26)$$

We can now identify the bracketed quantity in Eq. 25 as the energy of the continuous problem,

$$\begin{aligned}E&=KE+AE+GE\\&=\int_{-H}^{0}\int_{-\infty}^{\infty}\frac{1}{2}\rho\mathbf{v}^2\,\mathrm{d}x\mathrm{d}y+\int_{-H}^{0}\int_{-\infty}^{\infty}\frac{1}{2K}p^2\,\mathrm{d}x\mathrm{d}y\\&\quad+\int_{-\infty}^{\infty}\frac{1}{2}\rho g\eta^2\,\mathrm{d}x. \quad (27)\end{aligned}$$

Simply rewriting Eq. 25 as

$$\frac{dE}{dt}=\int_{-\infty}^{\infty}\frac{\partial b}{\partial t}\,p\Big|_{-H}\mathrm{d}x, \quad (28)$$

we see that the total mechanical energy is altered only by work done by tractions on the lower boundary. When the seafloor is rigid ($\partial b/\partial t=0$), energy is conserved. This will prove especially significant later in this work when we derive an analogous discrete energy balance that will be used to ensure stability of our numerical method. It is also worth noting that this energy balance is identical to that obtained when the small terms on the right sides of Eqs. 17 and 18 are retained.

2.2 Dispersion relation

Here, we briefly derive the dispersion relation for waves governed by Eqs. 16–18, neglecting the terms on the right side of Eqs. 17 and 18, in a rigid-bottomed ocean of uniform depth H (Fig. 1). Deriving the dispersion relation is important for characterizing wave modes, verifying that the approximations we introduced are consistent with standard treatments based on velocity potential and, for later use, as an exact solution in performing numerical convergence tests. We enforce the boundary and kinematic conditions given by Eqs. 20, 21, and 19, with $b(x,t)=0$. We write a homogeneous solution for pressure as

$$p(x,y,t)=\sin(kx)\sin(\omega t)\left[A\sinh(\bar{k}y)+B\cosh(\bar{k}y)\right], \quad (29)$$

for angular frequency ω, horizontal wavenumber k, and vertical wavenumber $\bar{k}=\sqrt{k^2-(\omega/c)^2}$. We can use the vertical momentum balance (17) to write an expression for vertical velocity:

$$v(x,y,t)=\frac{\bar{k}}{\rho\omega}\sin(kx)\cos(\omega t)\left[A\cosh(\bar{k}y)+B\sinh(\bar{k}y)\right]. \quad (30)$$

Imposing Eq. 21, with $b=0$, gives us one relationship between A and B:

$$A\cosh(\bar{k}H)-B\sinh(\bar{k}H)=0. \quad (31)$$

Another such relationship comes from time integrating Eq. 30 at the surface to get

$$\eta(x,t) = \frac{\bar{k}}{\rho\omega^2}\sin(kx)\sin(\omega t)A \tag{32}$$

and then applying Eq. 19, yielding

$$\frac{g\bar{k}}{\omega^2}A = B. \tag{33}$$

We combine Eqs. 31 and 33 and find that ω and k are related by the dispersion relation [21, 24]:

$$\omega^2 = g\bar{k}\tanh(\bar{k}H). \tag{34}$$

We are free to select $A = 1$, and thus, we can write the complete homogeneous solution as

$$\begin{aligned}
p(x,y,t) &= \sin(kx)\sin(\omega t)\left[\sinh(\bar{k}y) + \frac{g\bar{k}}{\omega^2}\cosh(\bar{k}y)\right],\\
v(x,y,t) &= \frac{\bar{k}}{\rho\omega}\sin(kx)\cos(\omega t)\left[\cosh(\bar{k}y) + \frac{g\bar{k}}{\omega^2}\sinh(\bar{k}y)\right],\\
u(x,y,t) &= \frac{k}{\rho\omega}\cos(kx)\cos(\omega t)\left[\sinh(\bar{k}y) + \frac{g\bar{k}}{\omega^2}\cosh(\bar{k}y)\right],\\
\eta(x,t) &= \frac{\bar{k}}{\rho\omega^2}\sin(kx)\sin(\omega t).
\end{aligned} \tag{35}$$

There are infinitely many modes that satisfy (35); that is, for a given k, there are infinitely many allowable ω_n. We identify the smallest value of ω_n as ω_0, corresponding to mode 0, the surface gravity wave as modified by compressibility. Higher modes, $\omega_1, \omega_2, \ldots$, correspond to ocean acoustic waves as modified by gravity, also known as acoustic gravity waves.

We first identify limiting values of phase velocity, $v_p = \omega/k$, in the limits of large and small wavelength surface gravity waves, $kH \ll 1$ and $kH \gg 1$, respectively. When compressibility effects are negligible, such that $\omega/ck \ll 1$, $\bar{k} \approx k$ and Eq. 34 reduces to

$$\omega^2 = gk\tanh(kH), \tag{36}$$

the well-known dispersion relation for surface gravity waves in an incompressible ocean of depth H [12]. In this incompressible limit, $v_p = \sqrt{gH}$ for large wavelengths and $v_p = \sqrt{g/k}$ for small wavelengths. For the compressible ocean problem with the dispersion relation given by Eq. 34, phase velocities in the large and small wavelength limits are approximated by

$$v_p = \sqrt{gH}\left(1 - \frac{1}{2}\frac{gH}{c^2}\right) \tag{37}$$

and

$$v_p = \sqrt{\frac{g}{k}}\left(1 - \frac{1}{4}\frac{g}{kc^2}\right). \tag{38}$$

These are modified versions of the phase velocities in the incompressible limit and include two key dimensionless parameters. The first, gH/c^2, quantifies the influence of compressibility on long-wavelength surface gravity waves [21]. For values of g, H, and c representative of the earth's oceans, $gH/c^2 \approx 0.02$. The second, g/kc^2, is similar to the first but more relevant for analysis of short wavelength waves ($kH \gg 1$); similarly, $g/kc^2 \ll 1$. This analysis shows that ocean compressibility has only a small effect on surface gravity waves.

For ocean acoustic waves, we first look at the case where gravity is neglected ($g = 0$). Here, the dispersion relation becomes $\cos\left(\sqrt{\omega^2/c^2 - k^2}H\right) = 0$. We see in Fig. 3 that in the long wavelength limit ($k \to 0$), v_p diverges for all modes $n \geq 1$ (they become vertically propagating sound waves), but that there are distinct cutoff frequencies ω_n. In the limit of zero gravity, $\omega_n = (2n-1)\pi c/2H$. When gravity is included, this is, to leading order in gH/c^2,

$$\omega_n = \frac{(2n-1)\pi c}{2H}\left[1 + \left(\frac{2}{(2n-1)\pi}\right)^2\frac{gH}{c^2}\right]. \tag{39}$$

In the short wavelength limit ($k \to \infty$), the phase velocity of each mode approaches c, but at a different rate for each n. For zero gravity, this can be quantified as $v_p = c\{1 + [(2n-1)\pi/2kH]^2/2\}$ to leading order in $1/kH$. When gravity is once again considered, this becomes, to leading order in the small parameters $1/kH$ and g/kc^2,

$$v_p = c\left[1 + \frac{1}{2}\left(\frac{(2n-1)\pi}{2kH}\right)^2\left(1 + 2\frac{g/kc^2}{kH}\right)\right]. \tag{40}$$

We observe that Eqs. 39 and 40 involve the small dimensionless parameters g/kc^2 and gH/c^2, indicating that the effect of gravity on ocean acoustic waves is slight. We note that the long and short wavelength limit approximations of the dispersion relation in this section should be slightly different from those predicted from the dispersion relation associated with the full treatment of the governing equations.

3 Discretized problem

Our aim is to numerically solve the governing equations in a provably stable and accurate way. Here, we consider the equivalent problem in only the vertical spatial dimension because this allows us to intuitively follow the development of the continuous problem. However, the analysis extends straightforwardly to two or three dimensions, and we present the 2-D case in the Appendix. We also neglect the terms on the right sides of Eqs. 17 and 18, though these terms can be included, if desired, without altering the discrete energy balance and stability proof presented below.

A field, say $p(y,t)$, is uniformly discretized on the interval $-H \le y \le 0$ by:

$$p_i(t) = p(y_i,t), \quad y_i = -H + ih, \quad i = 0, ..., N, \tag{41}$$

where $h = H/N$ is the grid spacing, y_0 is on the lower boundary, and y_N is on the upper boundary. We approximate the first derivative with an SBP difference operator $\boldsymbol{D}$ as follows [11, 22]:

$$\frac{\partial p}{\partial y} \approx \boldsymbol{D}\boldsymbol{p}, \quad \boldsymbol{D} = \boldsymbol{H}^{-1}\boldsymbol{Q}. \tag{42}$$

Grid data is contained in the vector $\boldsymbol{p}$, $\boldsymbol{H}$ is a symmetric positive definite matrix, and $\boldsymbol{Q}$ is an almost skew-symmetric matrix such that $\boldsymbol{Q}^T + \boldsymbol{Q} = \mathbf{diag}[-1\ 0\ \cdots\ 0\ 1]$. The second-order accurate SBP operator, for example, is given by

$$\boldsymbol{H} = h\,\mathbf{diag}\left[\frac{1}{2}\ 1\ 1\ \cdots\ 1\ \frac{1}{2}\right],$$
$$\boldsymbol{Q} = \frac{1}{2}\begin{bmatrix} -1 & 1 & & & \\ -1 & 0 & 1 & & \\ & \ddots & \ddots & \ddots & \\ & & -1 & 0 & 1 \\ & & & -1 & 1 \end{bmatrix}, \tag{43}$$

though we use higher order methods in this work. The value of summation by parts methods is that they are analogous to integration by parts. If we define the discrete and continuous inner products as

$$(u,v) = \int_{-H}^{0} u(y)v(y)\,\mathrm{d}y \quad \text{and} \quad (\boldsymbol{u},\boldsymbol{v})_h = \boldsymbol{u}^T\boldsymbol{H}\boldsymbol{v}, \tag{44}$$

we observe that

$$\left(p, \frac{\partial p}{\partial y}\right) = \int_{-H}^{0} p\frac{\partial p}{\partial y}\,\mathrm{d}y = \frac{1}{2}\left[(p|_0)^2 - (p|_{-H})^2\right], \tag{45}$$

$$\left(\boldsymbol{p}, \boldsymbol{H}^{-1}\boldsymbol{Q}\boldsymbol{p}\right)_h = \boldsymbol{p}^T\boldsymbol{Q}\boldsymbol{p} = \frac{1}{2}\boldsymbol{p}^T\left(\boldsymbol{Q}+\boldsymbol{Q}^T\right)\boldsymbol{p} = \frac{1}{2}\left(p_N^2 - p_0^2\right). \tag{46}$$

We use the SAT method [1] to weakly enforce boundary conditions. With SAT, boundary conditions are not enforced directly via injection (i.e., overwriting the grid data with the boundary data); instead, a penalty term is included in the semi-discrete equations to penalize the discrete equations for not satisfying the boundary conditions. With SBP and SAT, one can construct a discrete energy balance. For homogeneous boundary conditions, if the discrete energy can be shown to stay constant in time (or decrease due to a small numerical dissipation that vanishes as $h \to 0$), then the method is strictly stable [4]. Stability requires proper formulation of the penalty terms and choice of the penalty weights.

Time derivatives are discretized using a 4th-order low-storage Runge-Kutta method [2]. These methods are straightforward to apply, so in this paper, we focus solely on the semi-discrete problem.

Using the SBP operators described above, we discretize the governing Eqs. 16–18 in space without incorporating penalty terms at first:

$$\begin{aligned} \rho\frac{d\boldsymbol{v}}{dt} &= -\boldsymbol{D}\boldsymbol{p} = -\boldsymbol{H}^{-1}\boldsymbol{Q}\boldsymbol{p}, \\ \frac{1}{K}\frac{d\boldsymbol{p}}{dt} &= -\boldsymbol{D}\boldsymbol{v} = -\boldsymbol{H}^{-1}\boldsymbol{Q}\boldsymbol{v}. \end{aligned} \tag{47}$$

Multiplying the upper and lower equations of Eq. 47 by $\boldsymbol{v}^T\boldsymbol{H}$ and $\boldsymbol{p}^T\boldsymbol{H}$, respectively, and recognizing that $d(\boldsymbol{v}^T\boldsymbol{H}\boldsymbol{v})/dt = \boldsymbol{v}^T\boldsymbol{H}\,(d\boldsymbol{v}/dt) + (d\boldsymbol{v}^T/dt)\,\boldsymbol{H}\boldsymbol{v}$, we have

$$\begin{aligned} \frac{d}{dt}\left(\rho\boldsymbol{v}^T\boldsymbol{H}\boldsymbol{v}\right) &= \rho\frac{d\boldsymbol{v}^T}{dt}\boldsymbol{H}\boldsymbol{v} - \boldsymbol{v}^T\boldsymbol{Q}\boldsymbol{p}, \\ \frac{d}{dt}\left(\frac{1}{K}\boldsymbol{p}^T\boldsymbol{H}\boldsymbol{p}\right) &= \frac{1}{K}\frac{d\boldsymbol{p}^T}{dt}\boldsymbol{H}\boldsymbol{p} - \boldsymbol{p}^T Qv. \end{aligned} \tag{48}$$

We take the transpose of Eq. 47,

$$\rho\frac{d\boldsymbol{v}^T}{dt} = -\boldsymbol{p}^T\boldsymbol{Q}^T\boldsymbol{H}^{-1}, \quad \frac{1}{K}\frac{d\boldsymbol{p}^T}{dt} = -\boldsymbol{v}^T\boldsymbol{Q}^T\boldsymbol{H}^{-1}, \tag{49}$$

and insert them into Eq. 48:

$$\begin{aligned} \frac{d}{dt}\left(\rho\boldsymbol{v}^T\boldsymbol{H}\boldsymbol{v}\right) &= -\boldsymbol{p}^T\boldsymbol{Q}^T\boldsymbol{v} - \boldsymbol{v}^T\boldsymbol{Q}\boldsymbol{p}, \\ \frac{d}{dt}\left(\frac{1}{K}\boldsymbol{p}^T\boldsymbol{H}\boldsymbol{p}\right) &= \boldsymbol{v}^T\boldsymbol{Q}^T\boldsymbol{p} - \boldsymbol{p}^T\boldsymbol{Q}\boldsymbol{v}. \end{aligned} \tag{50}$$

Adding Eq. 50 to one another, dividing by two, and using the summation by parts property, we have

$$\begin{aligned} \frac{d}{dt}\left(\frac{\rho}{2}\boldsymbol{v}^T\boldsymbol{H}\boldsymbol{v} + \frac{1}{2K}\boldsymbol{p}^T\boldsymbol{H}\boldsymbol{p}\right) &= -\frac{1}{2}\left[\boldsymbol{p}^T(\boldsymbol{Q}^T+\boldsymbol{Q})\boldsymbol{v} + \boldsymbol{v}^T(\boldsymbol{Q}^T+\boldsymbol{Q})^T\boldsymbol{p}\right] \\ &= p_0v_0 - p_Nv_N. \end{aligned} \tag{51}$$

We recognize the left side of Eq. 51 as the discrete equivalent of the time derivative of the sum of KE and AE.

We define a discrete energy analogous to the continuous energy in Eq. 27:

$$E_h = \frac{1}{2}\left(\rho\boldsymbol{v}^T\boldsymbol{H}\boldsymbol{v} + \frac{1}{K}\boldsymbol{p}^T\boldsymbol{H}\boldsymbol{p} + \rho g\eta^2\right). \tag{52}$$

The discrete energy is not only a convenient mimic of the mechanical energy in the system, but it is also a positive definite functional of the solution at a given time. By introducing the correct penalty terms to Eq. 47 to enforce boundary conditions and repeating the preceding analysis, we can ensure that E_h is a nonincreasing function of time (and that any extra numerical dissipation vanishes as $h \to 0$). This will establish that our method is stable.

We now discuss boundary conditions in the discrete formulation of the problem. Since the governing Eqs. 16–18

are hyperbolic, we specify a number of boundary conditions equal to the number of characteristics propagating into the problem domain. The number of boundary conditions can be derived from a characteristic decomposition in the local coordinate system [10]. In one dimension, there is one characteristic that propagates upward and another that propagates downward. The characteristic variables associated with these waves, w^+ and w^-, respectively, are defined in terms of the pressure and velocity fields as

$$w^{\pm} = p \pm \rho c v. \tag{53}$$

These characteristics are simply sound waves with acoustic impedance ρc.

On the lower boundary, for example, we must set w^- to be equal to some value $\hat{w}^-$ determined by the physical boundary condition without modifying w^+. Here, and in what follows, the hat refers to variables that satisfy the boundary condition exactly. We focus on the homogeneous rigid bottom condition $v = 0$ here, although it is straightforward to extend the analysis to nonzero b as we considered in the continuous problem. We determine $\hat{w}^-$ from the following system of equations:

$$p_0 - \rho c v_0 = \hat{p}_0 - \rho c \hat{v}_0, \quad \hat{v}_0 = 0, \tag{54}$$

where v_0 and p_0 are the current grid values of velocity and pressure (which do not necessarily satisfy the boundary condition exactly). Similarly, we write the upper boundary condition as

$$p_N + \rho c v_N = \hat{p}_N + \rho c \hat{v}_N, \quad \hat{p}_N = \rho g \eta. \tag{55}$$

We now rewrite the discrete governing Eq. 47, this time including penalty terms to enforce the boundary conditions:

$$\begin{aligned} \rho \frac{d\boldsymbol{v}}{dt} &= -\boldsymbol{H}^{-1}\boldsymbol{Q}\boldsymbol{p} - \tau\rho c \boldsymbol{H}^{-1} \left[\left(v_0 - \hat{v}_0\right)\boldsymbol{e}_0 \right. \\ &\qquad \left. + \left(v_N - \hat{v}_N\right)\boldsymbol{e}_N \right], \\ \frac{1}{K}\frac{d\boldsymbol{p}}{dt} &= -\boldsymbol{H}^{-1}\boldsymbol{Q}\boldsymbol{v} - \tau\frac{c}{K}\boldsymbol{H}^{-1} \left[\left(p_0 - \hat{p}_0\right)\boldsymbol{e}_0 \right. \\ &\qquad \left. + \left(p_N - \hat{p}_N\right)\boldsymbol{e}_N \right], \end{aligned} \tag{56}$$

where τ is the dimensionless penalty parameter and $\boldsymbol{e}_i$ denotes an otherwise empty length-$(N+1)$ vector with a 1 in row i. This approach penalizes the incoming characteristic variable at each boundary by including specific forcing terms in the governing equations. We will see that by including penalty parameters of this form and selecting an appropriate value for τ, we arrive at an energy balance similar to Eq. 51 that conserves energy in the limit that $h \to 0$.

Following the procedure laid out in Eqs. 47–51, we arrive at

$$\begin{aligned} &\frac{1}{2}\frac{d}{dt}(\rho \boldsymbol{v}^T \boldsymbol{H}\boldsymbol{v} + \frac{1}{K}\boldsymbol{p}^T\boldsymbol{H}\boldsymbol{p}) = -p_N v_N \\ &-\tau[\rho c v_N(v_N - \hat{v}_N) + \frac{1}{\rho c}p_N(p_N - \hat{p}_N)] \\ &+p_0 v_0 - \tau[\rho c v_0(v_0 - \hat{v}_0) + \frac{1}{\rho c}p_0(p_0 - \hat{p}_0)]. \end{aligned} \tag{57}$$

From Eq. 54 and 55, we see that

$$\begin{aligned} p_N - \hat{p}_N &= p_N - \rho g \eta, \quad & v_N - \hat{v}_N &= -\frac{p_N - \rho g \eta}{\rho c}, \\ p_0 - \hat{p}_0 &= \rho c v_0, & v_0 - \hat{v}_0 &= v_0. \end{aligned} \tag{58}$$

The right-hand sides of Eq. 58 contain known quantities that can be evaluated to obtain the penalty terms in Eq. 56. Those penalty terms are added to the semi-discrete system of equations, but only at points on the boundaries of the domain. Selecting $\tau = 1$ and using Eq. 58, Eq. 57 becomes

$$\begin{aligned} &\frac{1}{2}\frac{d}{dt}(\rho \boldsymbol{v}^T \boldsymbol{H}\boldsymbol{v} + \frac{1}{K}\boldsymbol{p}^T\boldsymbol{H}\boldsymbol{p}) \\ &= -p_N v_N - [-v_N(p_N - \rho g\eta) + \frac{p_N}{\rho c}(p_N - \rho g \eta)] \\ &\qquad +p_0 v_0 - [\rho c v_0^2 - p_0 v_0] \\ &= -\frac{p_N^2}{\rho c} - \rho g \eta (v_N - \frac{p_N}{\rho c}) - \rho c v_0^2. \end{aligned} \tag{59}$$

Writing the discrete version of the ocean surface boundary condition from Eq. 20 as

$$\frac{d\eta}{dt} = \hat{v}_N, \tag{60}$$

and multiplying both sides of Eq. 60 by $\rho g \eta$, we can recognize the third term of E_h defined in Eq. 52:

$$\rho g \eta \hat{v}_N = \rho g \eta \frac{d\eta}{dt} = \frac{d}{dt}\left(\frac{1}{2}\rho g \eta^2\right). \tag{61}$$

We make use of Eq. 55 to rewrite Eq. 61 as

$$\rho g \eta (v_N + \frac{p_N - \rho g \eta}{\rho c}) = \frac{d}{dt}\left(\frac{1}{2}\rho g \eta^2\right). \tag{62}$$

Combining Eqs. 62 and 59, we obtain an expression for the time rate of change of the discrete energy:

$$\begin{aligned} \frac{dE_h}{dt} &= \rho g \eta \left(v_N + \frac{p_N - \rho g \eta}{\rho c}\right) - \frac{p_N^2}{\rho c} \\ &\quad -\rho g \eta \left(v_N - \frac{p_N}{\rho c}\right) - \rho c v_0^2 \\ &= -\frac{1}{\rho c}\left[p_N^2 - 2\rho g \eta p_N + (\rho g \eta)^2\right] - \rho c v_0^2 \\ &= -\frac{(p_N - \rho g \eta)^2}{\rho c} - \rho c v_0^2. \end{aligned} \tag{63}$$

We observe that E_h is a strictly decreasing function because the right side of Eq. 63 is nonpositive, and that $dE_h/dt = 0$

in the limit that the boundary conditions are exactly satisfied, i.e., $p_N = \rho g \eta$ and $v_0 = 0$. Thus, we have developed a method that has all the desirable stability and accuracy properties and can be used to model problems of interest.

The application of SBP and SAT extends to multiple dimensions in a straightforward manner because derivatives and boundary conditions in each direction are handled independently of each other. A general derivation for the 2-D elastic wave equation is presented by Kozdon et al. [8, 9], along with details on how to couple multiple blocks together along interfaces (both welded interfaces and frictional faults). In the remainder of this paper, we focus on 2-D problems.

4 Verification tests

Here, we describe two problems that we used to verify the stability and accuracy of the method and the linearized free surface boundary condition. For both problems, we neglect the terms on the right sides of Eqs. 17 and 18, so the predictions of our approximate model will have minor differences from the full treatment of the governing equations due to the neglect of those extra terms. The first test utilizes the analytical modal solution for a rigid-bottomed ocean presented earlier. Through convergence tests, we verify that the method provides solutions for both the tsunami and ocean acoustic modes with the expected order of accuracy. The second problem is more complex, featuring an ocean overlying an elastic solid, with a full seismic, acoustic, and tsunami wavefield generated by a prescribed slip distribution on a thrust fault. We verify that the seafloor uplift, in the long time limit, matches the known static elasticity solution for a buried dislocation. We also compare the evolution of surface gravity waves in our model to that predicted by a semi-analytical tsunami solution that assumes instantaneous tsunami excitation and propagation in an incompressible ocean. This allows us to isolate the effects of ocean compressibility and the finite rupture duration.

4.1 Uncoupled ocean problem

We consider the problem pictured in Fig. 2, a compressible ocean with height $H = 5$ km and width $L = 100$ km and the origin located on the upper left corner of the block. We enforce the following boundary conditions: $p(x, 0, t) = \rho g \eta(x, t)$, $v(x, -H, t) = 0$, and $p(0, y, t) = p(L, y, t) = 0$. A homogeneous solution to Eqs. 16–18 (not including terms on the right side) with this homogeneous set of boundary conditions is given by Eq. 35, with ω and $\bar{k}$ related by dispersion relation (34). Because the ocean has

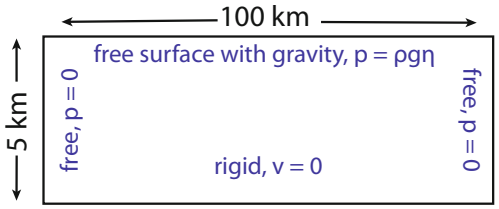

Fig. 2 Problem setup for Section 4.1, an uncoupled ocean with a free surface on top, a rigid seafloor, and zero pressure boundary conditions on the sides

a finite width, the horizontal wavenumber, k, must assume one of the following discrete values

$$k = \frac{\pi}{L} n, \quad n = 1, 2, \ldots \ . \tag{64}$$

In Fig. 3, we plot the discrete dispersion relation for the surface gravity mode in red and for the first five ocean sound wave modes in blue.

To test the numerical accuracy of the method, we ran this problem for various wavenumbers and modes. For each case, we ran the code for various grid spacings and compared the numerical solution with the exact solution after a set time. Error, ϵ, is measured in the discrete energy norm, defined as the square root of the energy-like quantity in Eq. 79 in the Appendix, but replacing fields with their difference from the exact solution (e.g., replacing $\boldsymbol{p}$ with

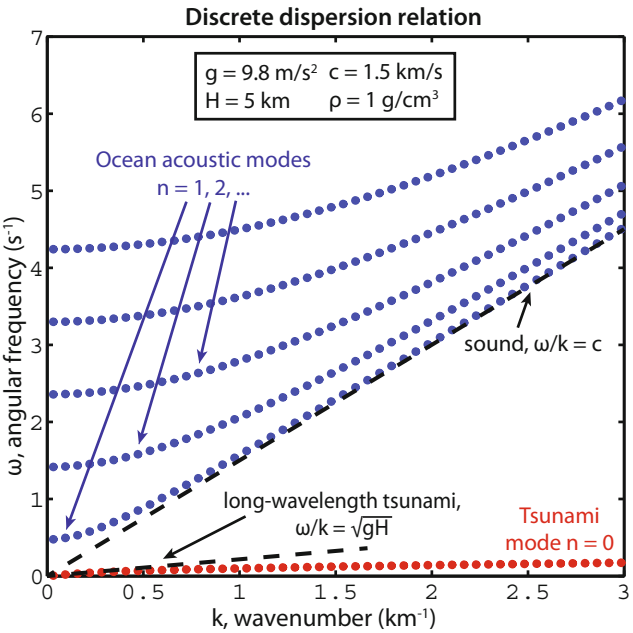

Fig. 3 Dispersion relation for discrete values of k in the uncoupled ocean problem plotted for modes 0 through 5. At small wavenumbers, the phase velocity, ω/k, of the tsunami mode approaches the shallow-water limit, $\sqrt{gH}$. At large wavenumbers, the phase velocity of the ocean acoustic modes approaches the sound speed, $c = \sqrt{K/\rho}$

Table 1 Error and rate estimates for the first two acoustic modes of the uncoupled ocean problem, for $k = \pi/(100\ \text{km})$

	Mode 1		Mode 2	
h (m)	Error	Rate	Error	Rate
250	7.75×10^{-5}		1.18×10^{-2}	
125	3.61×10^{-6}	4.4	4.21×10^{-4}	4.8
62.5	1.71×10^{-7}	4.4	1.70×10^{-5}	4.6
31.25	8.37×10^{-9}	4.4	7.64×10^{-7}	4.5

$\boldsymbol{p}_{\text{numerical}} - \boldsymbol{p}_{\text{exact}}$). In order to quantify the order of accuracy, we define the error rate between two discretizations with grid spacings h_1 and h_2 and errors ϵ_1 and ϵ_2 as

$$\text{Rate} = \frac{\log(\epsilon_1/\epsilon_2)}{\log(h_1/h_2)}. \tag{65}$$

We display error and rate estimates for modes 0, 1, and 2 for $k = \pi/(100\ \text{km})$ in Tables 1 and 2. Our method uses SBP operators that have interior accuracy $q = 6$ and boundary accuracy $r = q/2 = 3$, leading to a global accuracy of $p = r + 1 = 4$ [3]. The low-storage Runge-Kutta method we use is also accurate to order 4. We thus expect to calculate fourth-order rates in our convergence tests. Indeed, in Tables 1 and 2, we observe rates close to, and actually slightly greater than, four.

4.2 Coupled ocean and earth problem

We next present a coupled compressible ocean and elastic solid problem to demonstrate our ability to simultaneously model the full seismic, ocean acoustic, and surface gravity wavefield. The geometry and kinematic rupture parameter values appear in Fig. 4. A rectangular ocean with height $H = 5$ km and width $L = 400$ km overlays an elastic solid of the same width and height 100 km. A thrust fault of length $l = 50$ km intersects the center of the seafloor at point $(x = 0, y = -H)$ and at a dip angle of $\delta = 30°$. In the solid, we have P-wave speed $c_p = 8.0$ km/s, S-wave speed

Table 2 Error and rate estimates for the surface gravity mode of the uncoupled ocean problem, for $k = \pi/(100\ \text{km})$

	Mode 0	
h (m)	Error	Rate
250	2.44×10^{-7}	
166.7	4.30×10^{-8}	4.3
125	1.27×10^{-8}	4.2
100	4.98×10^{-9}	4.2
83.3	2.33×10^{-9}	4.2

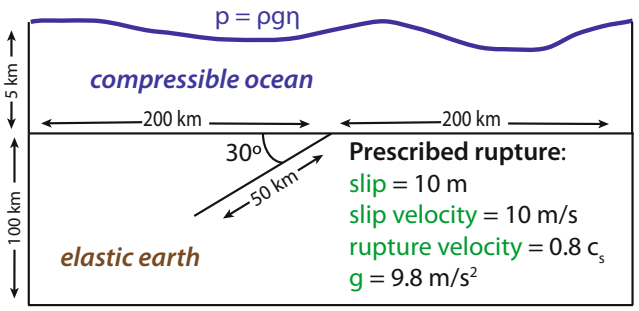

Fig. 4 Problem geometry and rupture parameters for the coupled ocean-earth problem in Section 4.2

$c_s = 4.6$ km/s, and $\rho = 3.2\ \text{g/cm}^3$, while in the ocean, we have $\rho = 1.0\ \text{g/cm}^3$, $c = 1.5$ km/s, and $g = 9.8\text{m/s}^2$.

On all external boundaries, we implement absorbing boundary conditions by setting the amplitude of the incoming characteristic variables to zero. For example, on the left boundary, we set $\hat{w}^+ = \hat{p} + \rho c\hat{u} = 0$ while maintaining the value of the outgoing characteristic, $\hat{w}^- = \hat{p} - \rho c\hat{u} = p - \rho cu$. We see that we can achieve this by assigning

$$\hat{p} = \frac{1}{2}(p - \rho cu), \qquad \hat{u} = \frac{1}{2}\left(u - \frac{1}{\rho c}p\right). \tag{66}$$

More details are given in the Appendix.

The earthquake rupture begins at the lower edge of the fault and propagates up to the seafloor at a constant rupture velocity, leaving behind it a uniform amount of slip. The prescribed slip velocity time function is described in [23]. The numerical method for enforcing the fault interface condition is described in detail in [9]. Fault slip generates seismic waves, ocean acoustic waves, and surface gravity waves. In Fig. 5, we plot the evolution of the sea surface η in space and time, noting some of the most prominent waves. For a more thorough discussion of these waves, see Kozdon and Dunham [7].

Next, we verify the seafloor displacement solution by comparison to the analytical solution for an edge dislocation that breaks the surface of an elastic half space. We expect this to be nearly an exact solution that our numerical solution should match as $t \to \infty$, except for very small differences due to the overlying ocean layer. Vertical seafloor displacement, $b(x)$, is given by [20]

$$\begin{aligned} b(x) &= \frac{s}{\pi}\left\{\sin\delta\left[\tan^{-1}(\zeta) - (\pi/2)\text{sgn}(x)\right] \right. \\ &\qquad \left. + \frac{\cos\delta + \zeta\sin\delta}{1+\zeta^2}\right\}, \\ \zeta &= \frac{x - l\cos\delta}{l\sin\delta}, \end{aligned} \tag{67}$$

where s is constant slip on the fault. This seafloor displacement profile is simpler than that observed in our numerical

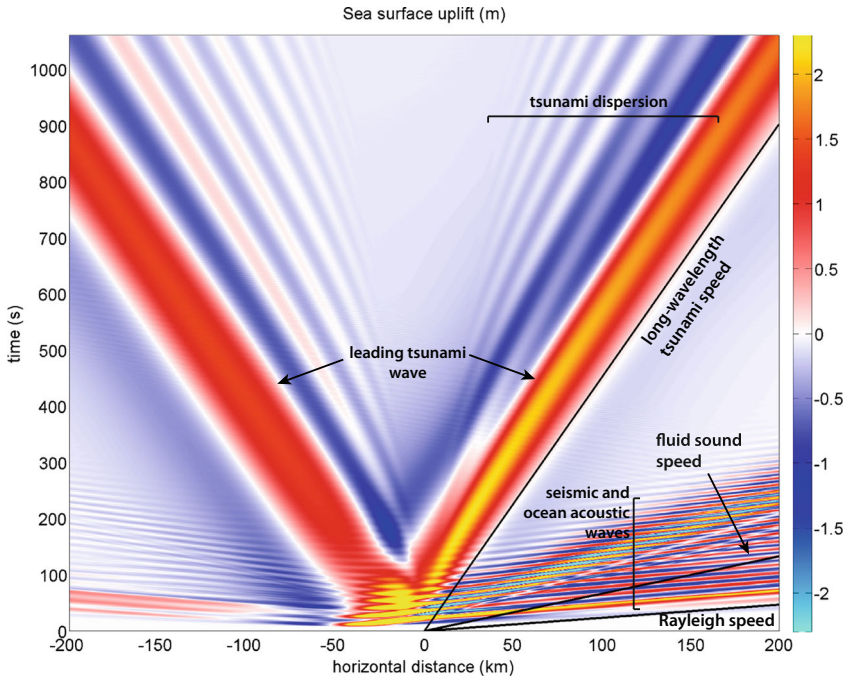

Fig. 5 Space-time plot of sea surface height η, illustrating the variety of waves generated by an earthquake on a thrust fault beneath the ocean. The black lines are drawn at the tsunami speed in the shallow water limit, $\sqrt{gH}$; the fluid sound speed, $c = \sqrt{K/\rho}$; and the Rayleigh wave speed, $0.919\, c_s$. After about 300 s, the bulk of the seismic and ocean acoustic waves have propagated out of the domain and only slower-traveling surface gravity waves remain. Note the dispersive tail to the tsunami

solution for multiple reasons. First, it is a static displacement, meaning that it is not caused by a time-dependent rupture, whereas our numerical problem ruptures over a number of seconds with a finite slip velocity. Second, the analytic solution assumes a half-space representation of the earth, subject to a free surface boundary condition, while the numerical problem is finite in both height and width and is overlaid by an ocean layer. Furthermore, inertial effects associated with the deformable solid and compressible ocean cause waves to ripple along the interface, causing the seafloor profile to change in time. Nevertheless, after the waves have propagated away, our predicted final seafloor displacement matches the analytical model remarkably well (Fig. 6).

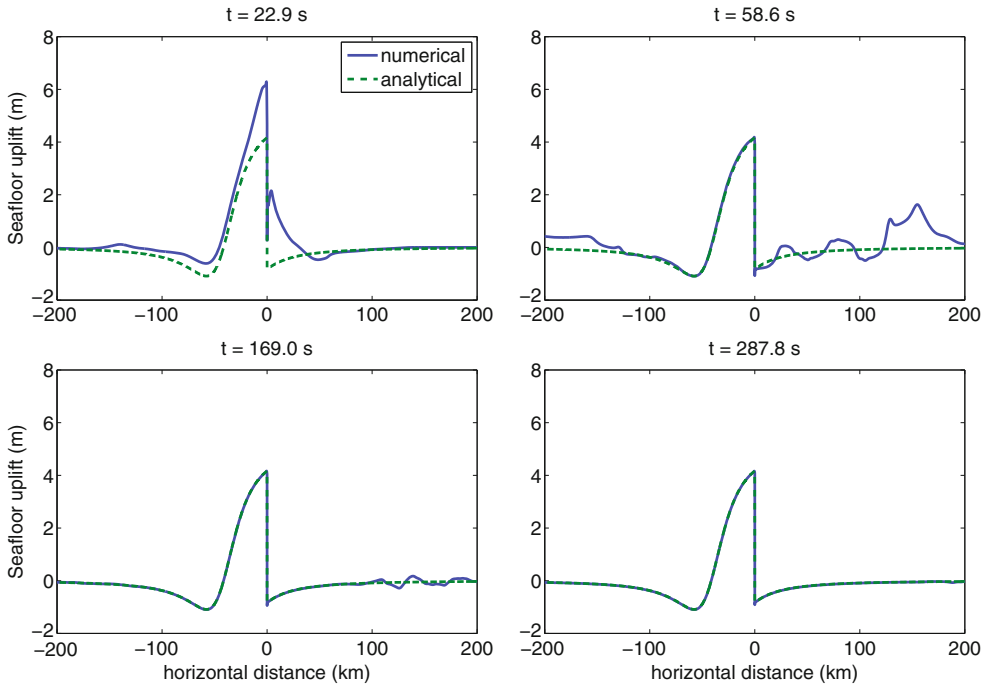

Fig. 6 Seafloor uplift snapshots from the static elasticity solution for a surface-breaking edge dislocation (*dashed green*) and the numerical solution (*solid blue*). After the seismic and ocean acoustic waves propagate out the domain, the models match very closely, as expected. Note the dynamic overshoot in the *upper left panel*

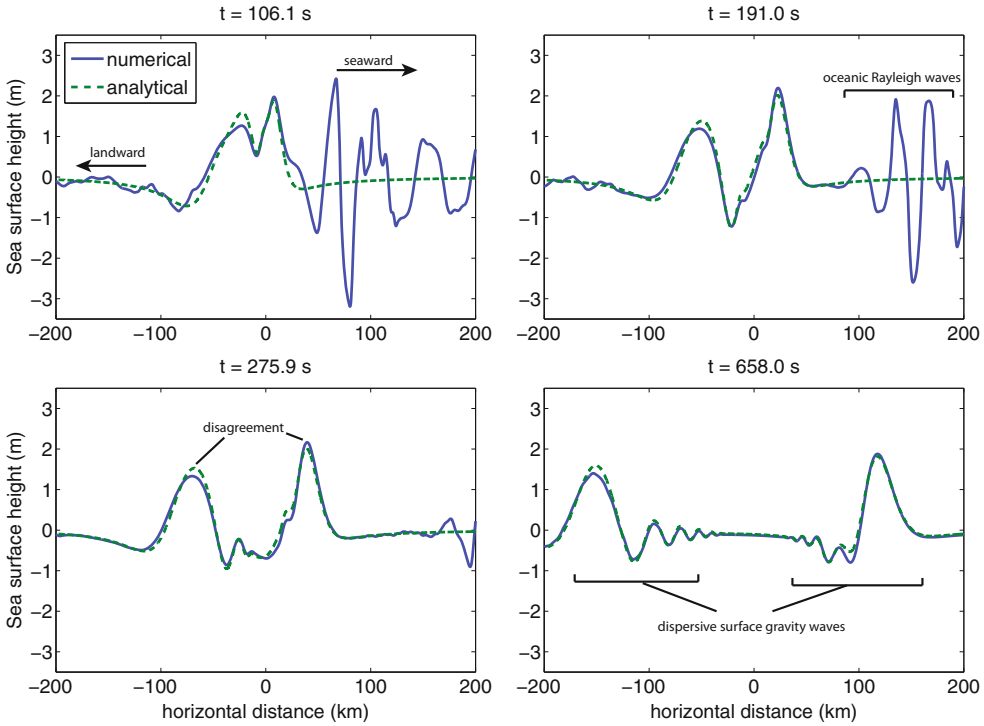

Fig. 7 Evolution of ocean surface, $\eta(x,t)$, in our simulation (*solid blue*) and as predicted by semi-analytical solution (*dashed green*) for tsunamis in an incompressible ocean generated by instantaneous uplift of the seafloor. Numerical solution curves are constant-time cross-sections of the space-time plot in Fig. 5. After the large-amplitude seismic and ocean acoustic waves propagate out of the domain, the dispersive surface gravity waves generally match. However, there are noticeable differences in the amplitude of the leading tsunami waves traveling both landward and seaward, which we attribute to the finite duration of the rupture and/or the compressibility of the ocean

We next examine the waves on the sea surface in more detail. In particular, we are interested in how the finite duration of the rupture and the compressibility of the ocean influence tsunami generation and propagation. The standard approach to tsunami modeling imposes seafloor uplift instantaneously beneath an incompressible ocean. The seafloor uplift translates directly into an initial condition on the sea surface η, but with short wavelength variations effectively filtered out due to nonhydrostatic response at length scales less than the ocean depth [5, 19].

This initial disturbance splits into two dispersive wave trains that we advance according to the dispersion relation for surface gravity waves in an incompressible ocean [12] using a semi-analytic Fourier spectral method. Because this incompressible ocean solution does not include compressibility effects or a finite, time-dependent rupture process, we do not expect perfect agreement. However, we anticipate the sea surface profile to match reasonably well once the seismic and ocean acoustic waves propagate out of the domain, leaving behind surface gravity waves at periods greater than those for which compressibility matters. We find that the numerical solution generally does match both the amplitude and wavelength content of the dispersive tsunami signal (Fig. 7). The largest difference is in the amplitude of the leading landward-traveling tsunami peak, though there is also a subtle difference in the seaward-traveling tsunami. Additional tests will need to be performed in order to better understand the source of these discrepancies, but they must arise from the compressibility of the ocean and/or the finite duration of the rupture process. This result could prove to be important, as the greatest discrepancy occurs in the most damaging part of the tsunami wavefield.

5 Conclusions

We have shown that by adopting a linearized dynamic free surface boundary condition in a finite difference framework, we can model the full seismic, ocean acoustic, and surface gravity wavefield all at once. We now have a powerful tool for better understanding tsunami generation and propagation in a compressible ocean with realistic geometries and rupture processes. Initial work is already being done to extend this method to three dimensions. A 3-D code would be of great use in solving tsunami problems for specific seafloor geometries because reflections and refractions of tsunami waves play a major role in determining hazard in many locales.

One component of our research effort involves looking for seismic and ocean acoustic signals that might help constrain the size of tsunami waves. Such signals could be recorded by ocean bottom pressure sensor networks and used to improve local tsunami early warning systems. With our simulation method, we can develop quantitative correlations between tsunami wave heights and the amplitudes, periods, and other features of seismic and acoustic waves. This preliminary study also establishes that, at least in some cases, the standard procedure for tsunami genera-

tion and propagation might incorrectly predict tsunami wave heights. Further work is required to determine if such differences arise in more realistic situations, but if they do, there would be obvious practical implications for tsunami hazard analysis.

Appendix

Discrete problem in two spatial dimensions

In Section 3, we discretize our problem and derive a numerical energy balance in the vertical spatial dimension. Here, we carry out the equivalent analysis in two dimensions. For some finite domain length L, we discretize the domain over $0 \le x \le L$ and $-H \le y \le 0$ and define the points

$$x_i = ih_x, \quad y_j = -H + jh_y, \tag{68}$$

where $i = 0, ..., N_x$, $j = 0, ..., N_y$, $h_x = L/N_x$, and $h_y = H/N_y$. Field values are stacked in the vectors $\boldsymbol{p}$, $\boldsymbol{u}$, and $\boldsymbol{v}$ and ordered as

$$\boldsymbol{p} = \begin{bmatrix} p_{00} & p_{01} & \cdots & p_{N_x N_y} \end{bmatrix}^T. \tag{69}$$

We write the governing Eqs. 16–18, not including the small terms on the right sides of Eqs. 17 and 18, in semi-discrete form using the SBP operators defined in Section 3:

$$\frac{d\boldsymbol{p}}{dt} = -K(\boldsymbol{D}_x\boldsymbol{u} + \boldsymbol{D}_y\boldsymbol{v}) + \boldsymbol{P}_T^p + \boldsymbol{P}_B^p + \boldsymbol{P}_L^p + \boldsymbol{P}_R^p, \tag{70}$$

$$\frac{d\boldsymbol{u}}{dt} = -\frac{1}{\rho}\boldsymbol{D}_x\boldsymbol{p} + \boldsymbol{P}_L^u + \boldsymbol{P}_R^u, \tag{71}$$

$$\frac{d\boldsymbol{v}}{dt} = -\frac{1}{\rho}\boldsymbol{D}_y\boldsymbol{p} + \boldsymbol{P}_T^v + \boldsymbol{P}_B^v, \tag{72}$$

$$\boldsymbol{D}_x = \boldsymbol{H}_x^{-1}\boldsymbol{Q}_x \otimes \boldsymbol{I}_y, \quad \boldsymbol{D}_y = \boldsymbol{I}_x \otimes \boldsymbol{H}_y^{-1}\boldsymbol{Q}_y, \tag{73}$$

where $\boldsymbol{H}_x^{-1}\boldsymbol{Q}_x$ is the 1-D SBP operator in the x-direction, $\boldsymbol{I}_x$ is the $(N_x+1)\times(N_x+1)$ identity matrix, and so on for $\boldsymbol{H}_y^{-1}\boldsymbol{Q}_y$ and $\boldsymbol{I}_y$. The Kronecker product of two matrices, $\otimes$, for matrix $\boldsymbol{A}$ of size $m \times n$ and matrix $\boldsymbol{B}$ of any size is

$$\boldsymbol{A} \otimes \boldsymbol{B} = \begin{bmatrix} a_{11}\boldsymbol{B} & \cdots & a_{1n}\boldsymbol{B} \\ \vdots & \ddots & \vdots \\ a_{m1}\boldsymbol{B} & \cdots & a_{mn}\boldsymbol{B} \end{bmatrix}. \tag{74}$$

Penalty terms $\boldsymbol{P}$ are chosen to properly enforce boundary conditions while allowing us to prove stability, where the superscripts p, u, and v refer to the penalized field and the subscripts T, B, L, and R refer to the top, bottom, left, and right edges of the domain. The penalty terms for the top boundary condition are

$$\boldsymbol{P}_T^p = -(\boldsymbol{I}_x \otimes c\boldsymbol{H}_y^{-1})[(\boldsymbol{p}_T - \hat{\boldsymbol{p}}_T) \otimes \boldsymbol{e}_T], \tag{75}$$

$$\boldsymbol{P}_T^v = -(\boldsymbol{I}_x \otimes c\boldsymbol{H}_y^{-1})[(\boldsymbol{v}_T - \hat{\boldsymbol{v}}_T) \otimes \boldsymbol{e}_T]. \tag{76}$$

Here, $\boldsymbol{p}_T$ and $\boldsymbol{v}_T$ are length (N_x+1) vectors containing the fields at grid points along the top boundary, $\hat{\boldsymbol{p}}_T$ and $\hat{\boldsymbol{v}}_T$ are length-(N_x+1) vectors of fields that exactly satisfy the top boundary condition, and $\boldsymbol{e}_T = [0 \cdots 0\ 1]^T$ is a vector of length (N_y+1). The hat variables are set in exactly the same manner as in the 1-D problem using Eq. 55 at each point on the boundary. No penalty term is applied to the u equation because characteristic variables associated with wave propagation normal to the top boundary involve only p and v.

As a second example, the penalty terms for the left boundary condition are

$$\boldsymbol{P}_L^p = -(c\boldsymbol{H}_x^{-1} \otimes \boldsymbol{I}_y)[\boldsymbol{e}_L \otimes (\boldsymbol{p}_L - \hat{\boldsymbol{p}}_L)], \tag{77}$$

$$\boldsymbol{P}_L^u = -(c\boldsymbol{H}_x^{-1} \otimes \boldsymbol{I}_y)[\boldsymbol{e}_L \otimes (\boldsymbol{u}_L - \hat{\boldsymbol{u}}_L)], \tag{78}$$

where the notation is similar to that for the top boundary. Note that for this boundary, the characteristic variables associated with wave propagation normal to the boundary involve p and u, rather than p and v, so penalties are applied to the p and u equations in this case. Similar penalty terms are introduced for the bottom and right boundaries.

We define a discrete 2-D energy similar to the 1-D energy in Eq. 52 and mirroring that of the continuous problem in Eq. 27:

$$E_h = \frac{1}{2}\left[\rho\boldsymbol{u}^T\boldsymbol{H}\boldsymbol{u} + \rho\boldsymbol{v}^T\boldsymbol{H}\boldsymbol{v} + \frac{1}{K}\boldsymbol{p}^T\boldsymbol{H}\boldsymbol{p} + \rho g\boldsymbol{\eta}^T\boldsymbol{H}_x\boldsymbol{\eta}\right], \tag{79}$$

where $\boldsymbol{\eta}$ is a vector of length (N_x+1) and $\boldsymbol{H} = \boldsymbol{H}_x \otimes \boldsymbol{H}_y$. Left multiplying Eq. 70 by $\boldsymbol{p}^T\boldsymbol{H}/K$, Eq. 71 by $\rho\boldsymbol{u}^T\boldsymbol{H}$, and Eq. 72 by $\rho\boldsymbol{v}^T\boldsymbol{H}$ and adding them together yields a discrete energy balance:

$$\begin{aligned} \frac{1}{K}\boldsymbol{p}^T\boldsymbol{H}\frac{d\boldsymbol{p}}{dt} + \rho\boldsymbol{u}^T\boldsymbol{H}\frac{d\boldsymbol{u}}{dt} + \rho\boldsymbol{v}^T\boldsymbol{H}\frac{d\boldsymbol{v}}{dt} &= \frac{d}{dt}\left(\frac{1}{2K}\boldsymbol{p}^T\boldsymbol{H}\boldsymbol{p} + \frac{\rho}{2}\boldsymbol{u}^T\boldsymbol{H}\boldsymbol{u} + \frac{\rho}{2}\boldsymbol{v}^T\boldsymbol{H}\boldsymbol{v}\right) \\ &= P_T + P_B + P_L + P_R, \end{aligned} \tag{80}$$

where the boundary work rates (P_T, P_B, P_L, and P_R) associated with the penalty terms can be obtained using the SBP property. By comparison to the energy balance for the continuous problem in Eq. 25, we anticipate that the right side of Eq. 81 must contain the gravitational potential energy rate,

$$\frac{d}{dt}\frac{1}{2}\int_0^L \rho g\eta^2 dx \approx \frac{d}{dt}\frac{1}{2}\rho g\boldsymbol{\eta}^T\boldsymbol{H}_x\boldsymbol{\eta}. \tag{81}$$

There will also be dissipation associated with the absorbing boundary conditions used on the left and right sides, as well as additional numerical dissipation that vanishes with mesh refinement. We now prove this, again providing details for the top and left boundaries.

The contribution from the top boundary is

$$P_T = -\boldsymbol{p}_T^T \boldsymbol{H}_x \boldsymbol{v}_T - \frac{1}{\rho c}\boldsymbol{p}_T^T \boldsymbol{H}_x \left(\boldsymbol{p}_T - \hat{\boldsymbol{p}}_T\right) - \rho c \boldsymbol{v}_T^T \boldsymbol{H}_x \left(\boldsymbol{v}_T - \hat{\boldsymbol{v}}_T\right). \quad (82)$$

We preserve the value of the upward-propagating characteristic variable using $\boldsymbol{p}_T + \rho c \boldsymbol{v}_T = \hat{\boldsymbol{p}}_T + \rho c \hat{\boldsymbol{v}}_T$ (see Section 3) to yield

$$P_T = -\hat{\boldsymbol{p}}_T^T \boldsymbol{H}_x \hat{\boldsymbol{v}}_T - \frac{1}{\rho c}(\boldsymbol{p}_T - \hat{\boldsymbol{p}}_T)^T \boldsymbol{H}_x (\boldsymbol{p}_T - \hat{\boldsymbol{p}}_T). \quad (83)$$

We then enforce the boundary condition $\hat{\boldsymbol{p}}_T = \rho g \boldsymbol{\eta}$, where $\boldsymbol{\eta}$ evolves according to $d\boldsymbol{\eta}/dt = \hat{\boldsymbol{v}}_T$. Now, the first term of Eq. 83 can be written

$$-\rho g \boldsymbol{\eta}^T \boldsymbol{H}_x \frac{d\boldsymbol{\eta}}{dt} = -\frac{1}{2}\rho g \frac{d}{dt}\left(\boldsymbol{\eta}^T \boldsymbol{H}_x \boldsymbol{\eta}\right), \quad (84)$$

which is the desired gravitational potential energy rate. We rewrite Eq. 81 as

$$\frac{dE_h}{dt} = P_T' + P_B + P_L + P_R \quad (85)$$

where P_T', the second term of Eq. 83, is negative semi-definite and goes to zero in the limit that the top boundary condition is exactly satisfied.

We next consider the left boundary term, which can be written as

$$P_L = \boldsymbol{p}_L^T \boldsymbol{H}_y \boldsymbol{u}_L - \frac{1}{\rho c}\boldsymbol{p}_L^T \boldsymbol{H}_y (\boldsymbol{p}_L - \hat{\boldsymbol{p}}_L) - \rho c \boldsymbol{u}_L^T \boldsymbol{H}_y (\boldsymbol{u}_L - \hat{\boldsymbol{u}}_L). \quad (86)$$

Using $\boldsymbol{p}_L - \rho c \boldsymbol{u}_L = \hat{\boldsymbol{p}}_L - \rho c \hat{\boldsymbol{u}}_L$, (86) becomes

$$P_L = \hat{\boldsymbol{p}}_L^T \boldsymbol{H}_y \hat{\boldsymbol{u}}_L - \frac{1}{\rho c}(\boldsymbol{p}_L - \hat{\boldsymbol{p}}_L)^T \boldsymbol{H}_y (\boldsymbol{p}_L - \hat{\boldsymbol{p}}_L). \quad (87)$$

Once again, the second term of Eq. 87 is negative semi-definite and vanishes with mesh refinement (i.e., when the boundary condition is exactly satisfied). The first term of Eq. 87 corresponds to the physical work rate on the boundary, which vanishes for either a free surface ($\hat{\boldsymbol{p}}_L = 0$) or rigid ($\hat{\boldsymbol{u}}_L = 0$) boundary. For our application simulations, we use an absorbing boundary condition constructed by setting the amplitude of the characteristic variable entering the domain to zero; that is, we set $\hat{\boldsymbol{p}}_L + \rho c \hat{\boldsymbol{u}}_L = 0$. It follows that $\hat{\boldsymbol{u}}_L = -\hat{\boldsymbol{p}}_L/\rho c$ and the first term of Eq. 87 becomes $-\hat{\boldsymbol{p}}_L^T \boldsymbol{H}_y \hat{\boldsymbol{p}}_L/\rho c$, which maximally dissipates energy as waves exit the domain through the left boundary. By performing similar analyses on P_B and P_R, we find that (85) dissipates energy slightly faster than the continuous problem, but exactly matches the energy balance of the continuous problem in the limit of mesh refinement. Thus, our 2-D numerical method is strictly stable.

References

1. Carpenter, M.H., Gottlieb, D., Abarbanel, S.: Time-stable boundary conditions for finite-difference schemes solving hyperbolic systems: methodology and application to high-order compact schemes. J. Comput. Phys. **111**(2), 220–236 (1994)
2. Carpenter, M.H., Kennedy, C.A.: Fourth-order 2N-storage Runge-Kutta schemes. NASA TM **109112** (1994)
3. Gustafsson, B.: The convergence rate for difference approximations to mixed initial boundary value problems. Math. Comput. **29**(130), 396–406 (1975)
4. Gustafsson, B., Kreiss, H.O., Oliger, J.: Time-dependent problems and difference methods, vol. 121. Wiley, New York (2013)
5. Kajiura, K.: The leading wave of a tsunami. Bull. Earthq. Res. Inst. **43**, 535–571 (1963)
6. Kozdon, J.E., Dunham, E.M.: Rupture to the trench: dynamic rupture simulations of the 11 March 2011 Tohoku earthquake. Bull. Seism. Soc. Am. **103**(2B), 1275–1289 (2013)
7. Kozdon, J.E., Dunham, E.M.: Constraining shallow slip and tsunami excitation in megathrust ruptures using seismic and ocean acoustic waves recorded on ocean-bottom sensor networks. Earth Planet. Sci. Lett. **396**, 56–65 (2014)
8. Kozdon, J.E., Dunham, E.M., Nordström, J.: Interaction of waves with frictional interfaces using summation-by-parts difference operators: weak enforcement of nonlinear boundary conditions. J. Sci. Comput. **50**(2), 341–367 (2012)
9. Kozdon, J.E., Dunham, E.M., Nordström, J.: Simulation of dynamic earthquake ruptures in complex geometries using high-order finite difference methods. J. Sci. Comput. **55**(1), 92–124 (2013)
10. Kreiss, H.O.: Initial boundary value problems for hyperbolic systems. Commun. Pure Appl. Math. **23**(3), 277–298 (1970)
11. Kreiss, H.O., Scherer, G.: Finite element and finite difference methods for hyperbolic partial differential equations. In: Mathematical aspects of finite elements in partial differential equations, pp. 195–212. Academic Press (1974)
12. Kundu, P., Cohen, I., Dowling, D.: Fluid mechanics. Academic Press, New York (2012)
13. Maeda, T., Furumura, T.: FDM simulation of seismic waves, ocean acoustic waves, and tsunamis based on tsunami-coupled equations of motion. Pure Appl. Geophys. **170**(1-2), 109–127 (2013)
14. Maeda, T., Furumura, T., Noguchi, S., Takemura, S., Sakai, S., Shinohara, M., Iwai, K., Lee, S.J.: Seismic and tsunami wave propagation of the 2011 off the pacific coast of Tohoku earthquake as inferred from the tsunami-coupled finite difference simulation. Bull. Seism. Soc. Am. **103**(2B), 1456–1472 (2013)
15. Maeda, T., Furumura, T., Sakai, S., Shinohara, M.: Significant tsunami observed at ocean-bottom pressure gauges during the 2011 off the Pacific coast of Tohoku earthquake. Earth Planets Space **63**, 803–808 (2011)
16. Marano, K.D., Wald, D.J., Allen, T.I.: Global earthquake casualties due to secondary effects: a quantitative analysis for improving rapid loss analyses. Nat. Hazards **52**(2), 319–328 (2010)
17. Matsumoto, H., Inoue, S., Ohmachi, T.: Some features of water pressure change during the 2011 Tohoku earthquake. Proceedings of the International Symposium on Engineering Lessons Learned from the 2011 Great East Japan Earthquake (2012)
18. Mori, N., Takahashi, T.: The 2011 Tohoku earthquake tsunami joint survey group: nationwide post event survey and analysis of the 2011 Tohoku earthquake tsunami, vol. 54 (2012)
19. Saito, T.: Dynamic tsunami generation due to sea-bottom deformation: analytical representation based on linear potential theory. Earth Planets Space **65**, 1411–1423 (2013)
20. Segall, P.: Earthquake and volcano deformation. Princeton University Press, Princeton (2010)

21. Sells, C.C.L.: The effect of a sudden change of shape of the bottom of a slightly compressible ocean. Philos. Trans. R. Soc. Lond. Ser. A, Math. Phys. Sci. **258**(1092), 495–528 (1965)
22. Strand, B.: Summation by parts for finite difference approximations for d/dx. J. Comp. Phys. **110**(1), 47–67 (1994)
23. Trugman, D.T., Dunham, E.M.: A 2d pseudodynamic rupture model generator for earthquakes on geometrically complex faults. Bull. Seism. Soc. Am. **104**(1), 95–112 (2014)
24. Yamamoto, T.: Gravity waves and acoustic waves generated by submarine earthquakes. Int. J. Soil Dyn. Earthq. Eng. **1**(2), 75–82 (1982)